Wave packets and Orr mechanism in turbulent jets

Gilles Tissot,[1,2,*] Francisco C. Lajús, Jr.,[2,3] André V. G. Cavalieri,[2] and Peter Jordan[4]
[1]*Institut de Mathématiques de Toulouse, Université Paul Sabatier, 31062 Toulouse, France*
[2]*Divisão de Engenharia Aeronáutica, Instituto Tecnológico de Aeronáutica, São José dos Campos, São Paulo 12228-900, Brazil*
[3]*Departamento de Engenharia Mecânica, Universidade Federal de Santa Catarina, Florianópolis, Santa Catarina 88040-900, Brazil*
[4]*Institut PPRIME, CNRS, University of Poitiers, ENSMA, 86000 Poitiers, France*
(Received 17 October 2016; published 18 September 2017)

Instability waves traveling within subsonic turbulent jets have a modal linear growth until approximatively the end of the potential core. At these stations it is believed that nonlinear and/or nonmodal effects become important and a mismatch appears between experimental measurements and linear models. In this paper the response of the linearized operator to nonlinearities treated here as an external forcing is found to be consistent with a simplified model of the Orr mechanism, supporting the idea that a nonmodal growth of disturbances occurs in the downstream region of the jet in response to the modeled nonlinear forcing.

DOI: 10.1103/PhysRevFluids.2.093901

I. INTRODUCTION

Wave packets are important features for the sound radiation of turbulent jets [1]. The downstream propagation of the Kelvin-Helmholtz mode, the solution of the near-nozzle local linear instability problem, matches hydrodynamic fluctuations until the end of the potential core [2]. Beyond this station, the linear model predicts a decay, while a growth is observed in experimental measurements. The linear solution also significantly underpredicts sound radiated by subsonic jets [3]. This mismatch has been understood to be due to the jitter of wave packets [4], whose statistical signature in the frequency domain is manifest in a decay of the coherence between two points as the distance between these is increased. As linear time-invariant wave-packet models lead invariably to unit two-point coherence, nonlinearity is believed to be the missing piece in the said models, and in this work we try to understand the underlying dynamic features from the perspective of deriving predictive reduced-order wave-packet models.

While the upstream region is dominated by a modal spatial growth of perturbations, underpinned by the Kelvin-Helmholtz mechanism [5], less is known about the dynamics of the downstream region, towards the end of the potential core, where the Kelvin-Helmholtz mode stabilizes and then decays. One hypothesis is that a nonmodal growth of disturbances seeded by nonlinearities becomes important in that region. Zhang [6] has performed an optimal disturbance analysis in which a sequence of matched optimal growth solutions was able to reproduce the experimental levels. In the same study a linearized Euler-equation calculation started at the end of the potential core using fluctuations taken directly from a large-eddy simulation (LES) supports the idea that the same nonmodal dynamics are present in the LES data. A locally parallel resolvent analysis has been performed by Tissot *et al.* [7] and the optimal responses match the experimental results in the downstream region of the jet, suggesting again a nonmodal mechanism as the homogeneous linear models fail in this region. In the same work, a four-dimensional variational (4DVar) data assimilation was performed in order to find the minimal external forcing, interpreted as the active nonlinearities, necessary to match the experimental data. A sensitivity analysis showed that the response to the forcing possesses traits typical of the Orr mechanism. We start from the results of that paper, which

*tissot.gilles@gmail.com

we compare with a simplified model of the Orr mechanism, in order to show that it is a plausible dynamic feature of wave packets forced by the background turbulence. Even if we rely in Sec. III on results from Tissot *et al.* [7], the paper is written as an independent study focusing on the presence of the Orr mechanism in the downstream region of turbulent jets.

Orr [8] has shown for inviscid linearized Couette flow that even though a modal instability mechanism does not exist for this flow, it is possible to obtain an initial-value problem leading to arbitrarily large disturbance growth. The associated eigenspectrum comprises a continuous branch of neutrally stable critical-layer modes [9–11], thus no modal instability can occur, but a non-normal growth can occur [12]. These studies have been performed in the context of hydrodynamic stability, where the flow linearization is considered strictly valid. This mechanism may nonetheless be active in fully turbulent flow; for instance, Jiménez [13,14] has educed the Orr mechanism in transient amplifications of disturbances in bursting events in the logarithmic layer of turbulent channel flow data. In the present paper, our aim is to explore wave-packet dynamics in turbulent jets and to illustrate the presence of the Orr mechanism in the downstream region where the flow is convectively stable.

Wave packets are most often defined in the Fourier domain. The Orr mechanism has already been described in frequency space by Sipp and Marquet [15], Dergham *et al.* [16], and Garnaud *et al.* [17]. The present work develops a quantitative approach to educe the Orr mechanism. We build a spatial Orr model equivalent to the temporal initial-value problem solved by Orr [8]. This consists, for a given frequency, in the spatial propagation of an inflow condition that develops in linearized, homogeneous shear flow; for a jet, the magnitude of such shear is given by a representative value in the downstream region, which is the focus of this study.

We present in Sec. II the temporal and spatial models of the Orr mechanism. Perturbations propagated by the spatial model are compared in Sec. III with jet wave packets forced by nonlinearities. The work is summarized in Sec. IV.

II. MODELS OF THE ORR MECHANISM

A. Basic equations

We recall in this section the methodology described by Orr [8] to solve the initial-value problem of the inviscid plane Couette flow, in two-dimensional Cartesian streamwise and wall-normal coordinates x and y, respectively. Consider the base flow defined by

$$U(y) = Sy \quad \text{for } y = [0,1], \tag{1}$$

where S is the magnitude of the shear. Small disturbances to this base flow can be characterised by the stream function ψ, whose evolution, considering the linearized inviscid flow equations, is described by

$$\left(\frac{\partial \cdot}{\partial t} - Sy\frac{\partial \cdot}{\partial x}\right)\nabla^2\psi = 0. \tag{2}$$

Streamwise and wall-normal velocity fluctuations can be obtained as $u = \partial\psi/\partial y$ and $v = -\partial\psi/\partial x$, respectively. Since the stream function and vorticity ξ are related by

$$\nabla^2\psi = -\xi, \tag{3}$$

we have

$$\left(\frac{\partial \cdot}{\partial t} - Sy\frac{\partial \cdot}{\partial x}\right)\xi = 0, \tag{4}$$

which simply states that vorticity fluctuations are advected with the local flow velocity. Modal solutions of the above equation are obtained assuming $\xi(x,y,t) = \hat{\xi}(y)e^{i(\alpha x-\omega t)}$ and are given as [9]

$$\hat{\xi}(y) = \delta(y - y_c), \tag{5}$$

where δ is the Dirac delta distribution and y_c is the critical point. The wave number α and frequency ω are related by $\omega = \alpha U(y_c)$; hence, the phase speed of disturbances is simply $U(y_c)$. We thus have a continuous spectrum of modal solutions comprised of neutral disturbances (real-valued ω and α) concentrated on a vortex sheet at $y = y_c$, which are advected by the local flow velocity [9]. The velocity (u,v) associated with these modes, where v is the solution of (A2) [9], decays exponentially with distance from the critical point (see Appendix B); thus, the resulting modes are clearly not orthogonal with respect to the standard $L2$ inner product applied to the velocity components, making possible algebraic growth or decay by constructive and destructive interferences.

B. Temporal model

Instead of considering a modal analysis, a nonmodal solution of an initial-value problem governed by Eq. (2) can be solved by considering the ansatz

$$\nabla^2\psi(x,y,t) = -\xi(x,y,t) = F(x - Syt, y), \tag{6}$$

with F an arbitrary function, determined by the initial conditions of the problem. This imposes that the vorticity disturbances, advected by local flow velocity, are tilted by the shear.

Starting from a given initial value $\psi_0(x,y) = \psi(x,y,t = 0)$, the right-hand side of (6) can be determined by

$$F(x,y) = \nabla^2\psi_0(x,y). \tag{7}$$

The solution can then been determined by solving the Poisson equation (6), which amounts to extracting the two velocity components from a known vorticity distribution. This model can be considered as *kinematic* in the sense that the solution at any time can be solved independently.

C. Spatial model

Now we construct a spatial version of the Orr mechanism, allowing computation of the Fourier-transformed component $\tilde{\psi}(x,y,\omega) = \int_{-\infty}^{\infty} \psi(x,y,t)e^{i\omega t}dt$ for each frequency ω, with a given inflow condition. This is done by starting from Eq. (6), which can be rewritten as

$$\frac{1}{2\pi}\int_{-\infty}^{\infty} \nabla^2\tilde{\psi}(x,y,\omega)e^{-i\omega t}dt = \frac{1}{2\pi}\int_{-\infty}^{\infty} \tilde{F}(\alpha,y)e^{i(x-Syt)\alpha}d\alpha, \tag{8}$$

with $\tilde{F}(\alpha,y) = \int_{-\infty}^{\infty} F(x,y)e^{-ix\alpha}dx$. To arrive at similar Fourier integrals on both the left- and right-hand sides, we perform the change of variables $\omega = Sy\alpha$,

$$\frac{1}{2\pi}\int_{-\infty}^{\infty} \nabla^2\tilde{\psi}(x,y,\omega)e^{-i\omega t}d\omega = \frac{1}{2\pi}\int_{-\infty}^{\infty} \tilde{F}\left(\frac{\omega}{Sy}, y\right)e^{i(\omega x/Sy-\omega t)}\frac{1}{Sy}d\omega, \tag{9}$$

and thus obtain

$$\nabla^2\tilde{\psi}(x,y,\omega) = \tilde{F}_2(y)e^{i(\omega x/Sy)}, \tag{10}$$

with $\tilde{F}_2(y) = \frac{1}{Sy}\tilde{F}(\frac{\omega}{Sy}, y)$. An interesting property is the scaling of the solution with $\frac{\omega x}{S}$. The temporal and spatial models are formally equivalent and the solution of the spatial problem can thus be rigorously defined as the Fourier transform of the solution of the temporal problem; however, the spatial formulation is adequate to study the development of disturbances in x, which potentially leads to transient growth in space. Similar to Eq. (7), we can determine the right-hand side of (10) at $x = 0$:

$$\tilde{F}_2(y) = \nabla^2\tilde{\psi}(0,y,\omega). \tag{11}$$

The solution $\nabla^2\tilde{\psi}(x,y,\omega)$, which amounts to the opposite of the Fourier-transformed vorticity $-\tilde{\xi}(x,y,\omega)$, can be determined once we provide $\tilde{\psi}(0,y,\omega)$ at the reference position $x = 0$, as well as $\partial^2\tilde{\psi}/\partial x^2(0,y,\omega)$. Alternatively, $\tilde{\xi}(0,y,\omega)$ can be directly specified. This inflow vorticity is

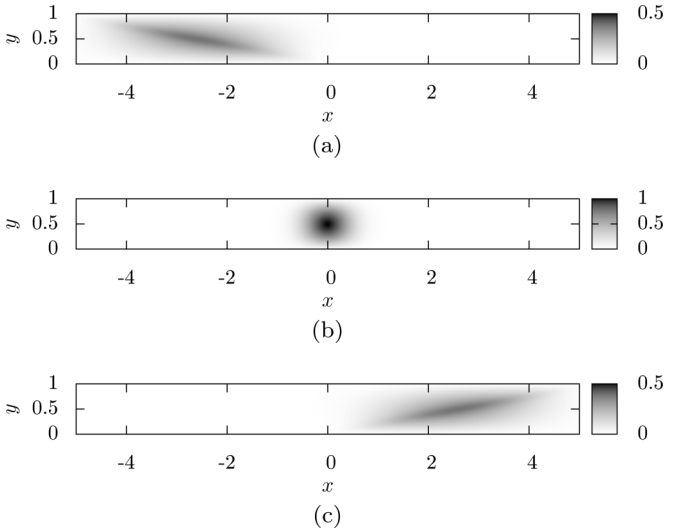

FIG. 1. Temporal Orr solution $\psi(x,y,t)$ with the initial condition (12) at (a) $t=-5$, (b) $t=0$, and (c) $t=5$.

propagated in space by the term $e^{i(\omega x/Sy)}$ representing convection of each vortex sheet by the local mean velocity.

Obtaining the velocity components from $\nabla^2\tilde{\psi}(x,y,\omega)$ can be done by using the Green's function given by Case [9]. Details are given in Appendix A. The procedure amounts to writing the vorticity as a sum of the neutral critical-layer modes in (5); each mode has distributions of the u and v components, which can then be superposed to form the full solution of the problem. This makes possible nonmodal growth by constructive or destructive interferences between theses modes, as will be seen next.

D. Comparison with numerical solutions

In this section, we verify, using a particular initial-value problem, the equivalence between the temporal and the spatial problems. We consider with the initial value

$$\psi_0(x,y) = \sin(ry)e^{-x^2/L^2}. \tag{12}$$

We have then

$$F(x-Syt,y) = -\frac{2L^2-4x^2+r^2L^4}{L^4}\sin(ry)e^{-x^2/L^2}. \tag{13}$$

We solve the Poisson equation numerically using a Fourier-Chebyshev pseudospectral method. Here $N_x = 1000$ streamwise wave numbers and $N_y = 201$ Chebyshev collocation points in the transverse direction have been used. We choose $r=\pi$ and $L=0.5$. The domain is $x=[-60,60]$ and $y=[0,1]$. Homogeneous Dirichlet boundary conditions are enforced to the stream function at $y=0$ and $y=1$, which implies free-slip boundary conditions and zero-average streamwise mass flux of the perturbation. We take $S=1.0365$ in order to be consistent with the jet study at St $=0.6$ in Sec. III. The numerical solution of the temporal Orr model is shown in Fig. 1. As expected, we observe a tilting of the perturbation by the shear, with an amplitude of ψ that grows and decays with time.

The equivalent spatial model can be built by taking

$$\tilde{F}(\alpha,y) = -\sqrt{\pi}L(\alpha^2+r^2)\sin(ry)e^{-L^2\alpha^2/4} \tag{14}$$

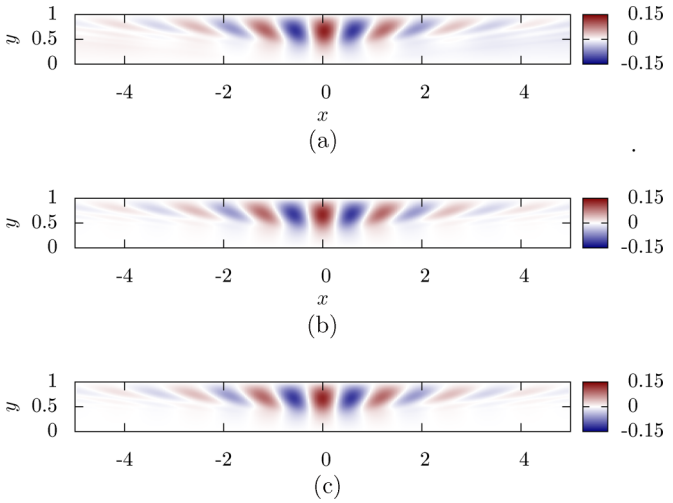

FIG. 2. Spatial Orr solution Re[$\tilde{\psi}(x,y,\omega)$], with $\omega = 3.77$, for (a) the Fourier transform of the temporal solution $\psi(x,y,t)$, (b) the spatial model solved numerically, and (c) the spatial model solved using Green's functions.

and then

$$\tilde{F}_2(y) = -\frac{\sqrt{\pi}L}{Sy}\left[\left(\frac{\omega}{Sy}\right)^2 + r^2\right]\sin(ry)e^{-L^2(\omega/Sy)^2/4}. \tag{15}$$

Figure 2 displays a comparison between $\tilde{\psi}(x,y,\omega)$ for $\omega = 3.77$ (i.e., $\mathrm{St} = \omega/2\pi = 0.6$) computed by performing the Fourier transform of the temporal solution [Fig. 2(a)] and solving Eq. (11) numerically with the Fourier-Chebyshev method [Fig. 2(b)]. Figure 2(c) shows a solution of Eq. (11) obtained using the Green's function of Case [9], as explained in Appendix A. We observe a tilting of the solution in space and an amplitude growth and decay with a maximum at $x = 0$. As discussed in the preceding section, since the spectrum is composed of neutral modes, the observed growth is necessarily nonmodal and can be seen to result from constructive or destructive interferences between the different vorticity waves, or critical-layer modes, as they are advected with the local flow velocity. The observed tilting of the perturbation is a direct consequence of the term $e^{i(\omega x/Sy)}$ in Eq. (10), translating the fact that perturbations are advected faster in high-speed regions than in low-speed regions.

The good agreement between the solutions validates the methods. We can see in this example how the solution of the initial-value problem manifests in the Fourier-domain solution as a tilting of the structure in space. This gives us confidence in interpreting the tilting in space of a harmonic perturbation as an effect of the Orr mechanism.

III. ORR MECHANISM IN TURBULENT-JET WAVE PACKETS

In order to determine if an Orr mechanism is active in turbulent-jet wave packets, we start from results established by Tissot *et al.* [7]. Based on a 4DVar data assimilation combined with the parabolized stability equations (PSEs), the sensitivity of the PSE solution, for a $M = 0.4$ jet, with respect to an external forcing, interpreted as the active nonlinearities, has been determined. Details of the jet measurements are given by Cavalieri *et al.* [2]. An optimal infinitesimal forcing is obtained, where optimality is such that the corresponding linearized flow response matches the first proper orthogonal decomposition (POD) mode of the experimental power spectral density (PSD) of the velocity fluctuations. The procedure is thus optimal in finding the forcing terms missing in linear

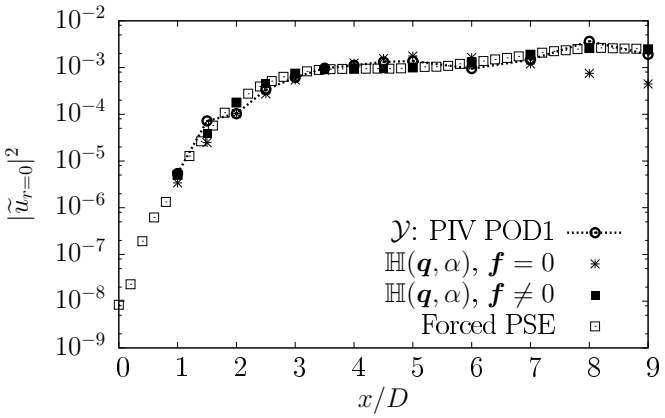

FIG. 3. Centerline streamwise fluctuating energy at St = 0.6 for the first POD mode of PIV measurements (○), the observation operator for the homogeneous PSE (∗), the observation operator for the forced PSE (■), and the PSE solution of the forced PSE (□).

wave-packet models, such as linear PSE; the forcing is then interpreted as the relevant missing nonlinear effects.

The parabolized stability equations [18] model the evolution of disturbances over a slowly varying base flow, considered here as the mean flow of the jet. The formulation used here is similar to that used in previous works [2,19,20]. The assumption of a slowly varying base flow allows decomposition of the perturbation associated with mode (ω,m) into slowly and rapidly varying (wavelike) parts [18]

$$\tilde{\boldsymbol{q}}_{\omega,m}(x,r) = \boldsymbol{q}(x,r)\exp\left(i\int_0^x \alpha(\xi)d\xi\right), \tag{16}$$

where $\boldsymbol{q}(x,r)$ is the slowly varying part and $\exp(i\int_0^x \alpha(\xi)d\xi)$ the wavelike part. The (ω,m) index is dropped for compactness and we focus on the azimuthal mode $m=0$, which is the most acoustically efficient for low frequencies [2,21]. The decomposition (16) is introduced into the compressible Navier-Stokes equations. The nonlinear terms are then neglected, assuming small perturbations over the experimental mean flow. The first axial derivatives of α and second axial derivatives of $\boldsymbol{q}$ are neglected, assuming a slow variation of these variables in the streamwise direction. We consider as well an external forcing term

$$\tilde{\boldsymbol{f}}_{\omega,m}(x,r) = \boldsymbol{f}(x,r)\exp\left(i\int_0^x \alpha(\xi)d\xi\right), \tag{17}$$

representing the effect of nonlinearities, similarly to what is done in resolvent analysis applied to turbulent flows [7,22]. We finally obtain equations of the form

$$E\frac{\partial \boldsymbol{q}}{\partial x} + (A+\alpha B)\boldsymbol{q} = \boldsymbol{f}, \quad \int_0^\infty \boldsymbol{q}\cdot\frac{\partial \boldsymbol{q}}{\partial x} r\,dr = 0, \tag{18}$$

where the first equation is used to obtain the evolution of $\boldsymbol{q}$ and the second is a restriction ensuring that $\boldsymbol{q}$ is a slowly varying function [18].

The objective of 4DVar data assimilation is to seek $\boldsymbol{f}$ minimizing

$$\mathcal{J}(\boldsymbol{q},\alpha,\boldsymbol{f}) = \frac{1}{2}\int_0^L \|\mathbb{H}(\boldsymbol{q},\alpha)-\mathcal{Y}\|^2 dx, \tag{19}$$

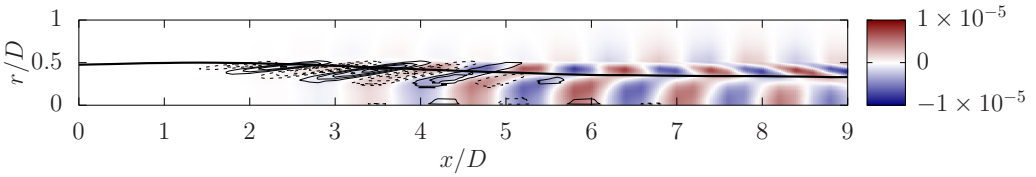

FIG. 4. Infinitesimal forcing and associated response. Colors are $\mathrm{Re}(\delta\tilde{\boldsymbol{q}}^u)$ and isocontours are $\mathrm{Re}(\delta\tilde{\boldsymbol{f}}^u)$; solid lines are for positive values and dashed lines are for negative values. The thick solid line is the critical-layer position.

where $\mathbb{H}(\boldsymbol{q},\alpha)$ is an observation operator allowing passage from the state space to the observation space

$$\mathbb{H}(\boldsymbol{q},\alpha) = Q\left|\boldsymbol{q}\exp\left(i\int_0^x \alpha(\xi)d\xi\right)\right|^2 \tag{20}$$

and $\mathcal{Y}$ is the PSD of streamwise and radial velocity measurements. Here Q is a rectangular matrix of 0's and 1's, whose rows contain a 1 in order to select the components and the radial positions that are observed, here the axial and radial velocities for the positions where there are available time-resolved particle image velocimetry (PIV) results. The $\mathcal{J}$ function is thus a metric for deviations of the PSE solution in Eq. (18) from experimental measurements. Sensitivity of $\mathcal{J}$ with respect to $\boldsymbol{f}$ is determined by an adjoint method.

As an illustration, Fig. 3, presenting results extracted from [7], shows the PSD of the streamwise velocity component at the jet centerline, with a comparison between measurements, linear PSEs, and the PSE forced by the converged 4DVar solution. The ability of the optimally forced PSE to reproduce experimental measurements gives us confidence in further interpretations. In the following, we focus on sensitivity results around $\boldsymbol{f} = 0$, i.e., the first iteration of the 4DVar algorithm. This is the reason why no penalty term to the forcing is used in Eq. (19).

Let $\delta\tilde{\boldsymbol{f}} = -(\partial\mathcal{J}/\partial\boldsymbol{f})\exp(i\int_0^x \alpha(\xi)d\xi)$ be the optimal infinitesimal forcing. We define the infinitesimal response $\delta\tilde{\boldsymbol{q}} = \tilde{\boldsymbol{q}}^f - \tilde{\boldsymbol{q}}^h$, where $\tilde{\boldsymbol{q}}^h$ is the solution of the homogeneous PSE (i.e., the linear wave-packet model) and $\tilde{\boldsymbol{q}}^f$ is the solution of the PSE forced by $\gamma\delta\tilde{\boldsymbol{f}}$, with $\gamma = 10^{-8}$. We here simplify the notation used by Tissot *et al.* [7], dropping (m,ω) indices. We present results for $\mathrm{St} = 0.6$, which is a representative case; results for other Strouhal numbers are shown in Appendix C.

The response to forcing $\delta\tilde{\boldsymbol{q}}$ comprises a tilting of the perturbations, visible in Fig. 4, associated with a growth and decay of the vertical velocity magnitude (Fig. 5). These are qualitative traits of the Orr mechanism, and we propose to compare this response more quantitatively with the spatial model of the Orr mechanism developed in the preceding section. We focus on the quantities at the critical layer, i.e., the position where the phase speed of the perturbation matches the mean flow velocity. As pointed out by Lindzen [23], this is the position where the wave travels with the local flow velocity and thus where the Orr mechanism is expected to be active. The phase velocity is defined as $c = \frac{\omega}{\alpha}$, where α is the local wave number predicted by the PSE. We neglect in that sense the slow phase variations of the slowly varying part of the PSE solution.

We will approximate the jet flow in the downstream region by an inviscid bidimensional Couette flow. This approximated Couette flow is clearly a minimalistic description of the base flow, but one that nonetheless possesses the same salient features of the jet at the critical layer; the shear S is taken for the axial position where the vertical velocity $|\delta\tilde{\boldsymbol{q}}^v|^2$ of the PSE response is maximum, which corresponds at $\mathrm{St} = 0.6$ to $(x_{\mathrm{CL}}/D = 6, r_{\mathrm{CL}}/D = 0.35)$ (see the red point in Fig. 5). This is located in a region where the jet has a more homogenized shear and the mean profile has developed to a more distributed shape. The shear is $S = -1.0365$ at $\mathrm{St} = 0.6$ and we use the perturbation inflow radial profile given by $\delta\tilde{\boldsymbol{q}}$ from the PSE, with the same local streamwise wave number $\alpha = 5.0$ in order to have access to the local phase velocity. To ensure consistency between the Orr model and

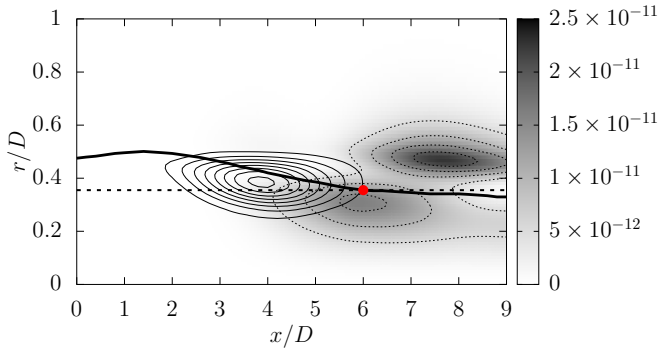

FIG. 5. Infinitesimal forcing and associated response. Colors are $|\delta\tilde{\boldsymbol{q}}^v|^2$ and isocontours are $|\delta\tilde{\boldsymbol{f}}^v|^2$. The red point indicates the position where the conditions (shear, mean flow velocity, inflow profile, and local wave number) are used for building the Couette flow approximation. The dashed line is the line where the PSE and the Orr model are compared.

jet flow, a linear base-flow profile $U_{\mathrm{Orr}}(y) = S(1-y)$ is considered with $y = [0,1]$ and S prescribed above. The PSE perturbation profile at x_{CL} is translated in such a way the critical-layer positions of the jet (r_{CL}) and the Orr model ($y_{\mathrm{CL}} = c/S$) correspond. It is then interpolated in the new domain to define the inflow perturbation. Thus, we enforce, for instance, $v^{\mathrm{Orr}}(y - y_{\mathrm{CL}}) = v^{\mathrm{PSE}}(r - r_{\mathrm{CL}})$.

We define moreover the tilting angle, in the same way as in [13], as the angle of isophase lines

$$\phi = \frac{\pi}{2} - \arctan\left(\frac{\partial\theta/\partial y}{\partial\theta/\partial x}\right), \tag{21}$$

where θ is the phase of the streamwise component of the perturbation. For qualitative comparison, the streamwise component of the Orr solution is shown in Fig. 6. A perfect match between this simplified solution and the PSE result is not expected, especially for positions far from the specified inflow or far from the critical layer. We can however observe qualitative similarities of the axial velocity between the PSE and Orr models, especially the observed tilting angle.

In Fig. 7, a comparison of the PSD of the vertical velocity $|v|^2$ and of the tilting angle ϕ between the model of the Orr mechanism and $\delta\tilde{\boldsymbol{q}}$ from the PSE is shown along a line drawn in Fig. 5. This line is defined by $r/D = r_{\mathrm{CL}}/D = \mathrm{const}$ for the PSE and for the Orr model the corresponding values are taken where the local flow velocity matches that of the PSE, i.e., $y_{\mathrm{CL}} = 0.27$ at $\mathrm{St} = 0.6$ (see Fig. 6). The good agreement allows us to say that the response to the optimal nonlinear forcing is amplified by an Orr mechanism in the downstream region of the jet.

The same procedure has been performed for the homogeneous wave packet $\tilde{\boldsymbol{q}}^h$ in Fig. 8. The perturbation computed by the linear PSE is propagated using the spatial Orr model. The inflow is this time calibrated at $x/D = 4$, the maximum value position of $|\tilde{\boldsymbol{q}}^{h,v}|^2$. In the linear PSE case, the PSD

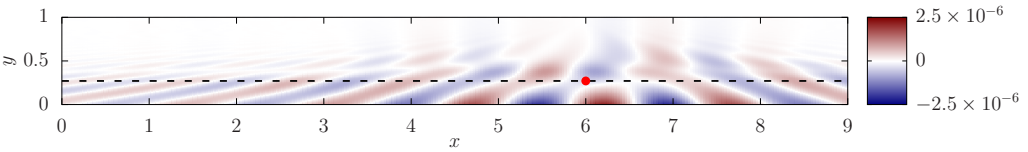

FIG. 6. Spatial Orr solution [Re(u)] with inflow calibrated on the jet wave-packet response $\delta\tilde{\boldsymbol{q}}$ at $x/D = 6$. The red point indicates the position where the conditions from the PSE (shear, mean flow velocity, inflow profile, and local wave number) are used for building the Couette flow approximation. The dashed line is the line where the PSE and Orr model are compared.

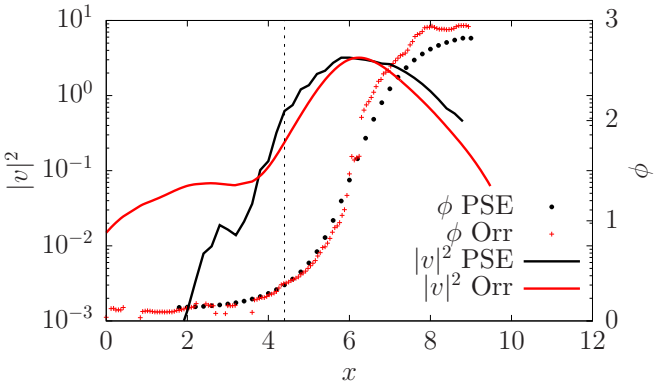

FIG. 7. Comparison between the PSE response to the sensitivity forcing and the spatial Orr model. For the PSE, we take the values of $|v|^2$ and tilting angle along $r/D = 0.35$, the critical-layer position at $x/D = 6$. For the Orr model, the values are taken at $y = \omega/S\alpha = 0.27$ such that the mean-flow velocity corresponds to the one at the critical layer in the PSE. The vertical dashed line is the position where the PSE has neutral growth.

$|v|^2$ does not correspond to the Orr mechanism as well as in the case of the forcing response. This is an expected result since the linear PSE is subject to an exponential growth in the upstream region, while the Orr model contains only neutral modes, which when acting together can lead at best to an algebraic growth. However, the tilting angles ϕ are similar. The perturbation is tilted between $x/D = 4$ and $x/D = 6$ as soon as the wave packet becomes neutral, and a critical layer appears (quasireal phase speed c). This good prediction by the Orr model can be explained by the fact that critical-layer modes are also active in the downstream region of the linear PSE. This is corroborated by the fact that in a locally parallel stability analysis, at these axial positions, the Kelvin-Helmholtz mode has already joined the critical-layer branch as we move downstream [5]. By comparing the results for unforced and forced wave packets, we interpret the role of nonlinearities as an additional forcing that intensifies the activity of the critical-layer modes, which then leads to growth in space via the Orr mechanism.

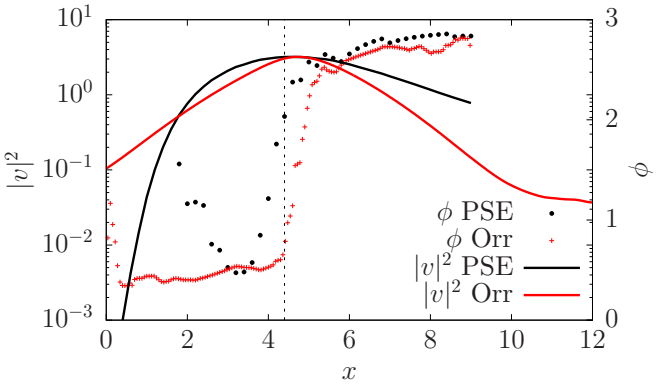

FIG. 8. Comparison between the linear PSE and the spatial Orr model. For the PSE, we take the values of $|v|^2$ and tilting angle along $r/D = 0.4$, the critical-layer position at $x/D = 4.6$. For the Orr model, the values are taken at $y = \omega/S\alpha = 0.47$ such that the mean-flow velocity corresponds to the one at the critical layer in the PSE. The vertical dashed line is the position where the PSE has neutral growth.

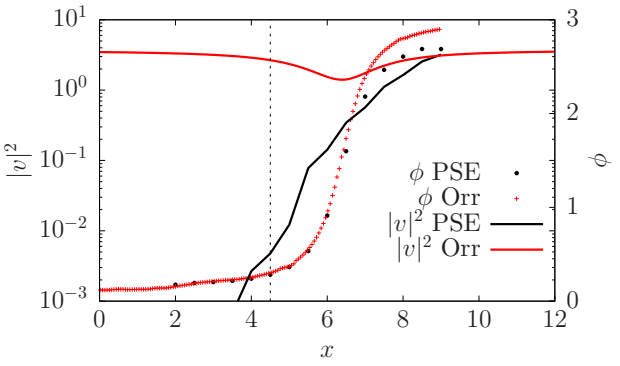

FIG. 9. Similar results to Fig. 7, comparing $\delta\boldsymbol{q}$ from the PSE with the spatial Orr model for St = 0.5.

The fact that Couette flow is able to reproduce the same features as the jet in the downstream region indicates that the critical-layer modes play a central role in that region.

IV. CONCLUSION

We have developed a model of the spatial Orr mechanism, defined in the frequency domain, that is equivalent to the standard temporal model. The model allows a quantitative comparison of wavy disturbances with the spatial Orr mechanism, in a manner similar to that used to compare intermittent events in wall-bounded flows with their temporal equivalents [13,14].

We have compared the response of PSEs subject to an optimal infinitesimal forcing, representing the effect of salient nonlinearities [7], with the propagation of the perturbation by the simplified Orr model. Good agreement suggests that in the region downstream of the potential core, wave packets in jets are submitted to nonlinearities induced either by background turbulence or by nonlinear wave-packet interactions and that the associated response is amplified by the Orr mechanism.

Critical-layer modes, when acting together to produce constructive and destructive combinations, are the essence of the nonmodal transient growth described by the Orr mechanism. These modes, which appear explicitly in the solution of the spatial model of the Orr mechanism, play a central role in the wave-packet dynamics. They are already active in homogeneous linear wave packets, and background turbulence intensifies their contribution by additional forcing, which becomes dominant when the Kelvin-Helmholtz mode becomes stable due to the base-flow divergence.

APPENDIX A: RESOLUTION USING GREEN'S FUNCTIONS

A solution of the Poisson equation (10) can be found using Green's functions. First, let us perform a Fourier transform of (10) in the streamwise direction

$$\left(-\alpha^2+\frac{\partial^2.}{\partial y^2}\right)\hat{\psi}(\alpha,y,\omega)=\tilde{F}_2(y)\int_{-\infty}^{+\infty}e^{i(\omega x/Sy-\alpha x)}dx=\tilde{F}_2(y)2\pi\delta\left(\frac{\omega}{Sy}-\alpha\right) \tag{A1}$$

Let us now define the Green's function $G(y,y',\alpha)$, the solution of

$$\left(-\alpha^2+\frac{\partial^2.}{\partial y^2}\right)G(y,y',\alpha)=\delta(y-y'). \tag{A2}$$

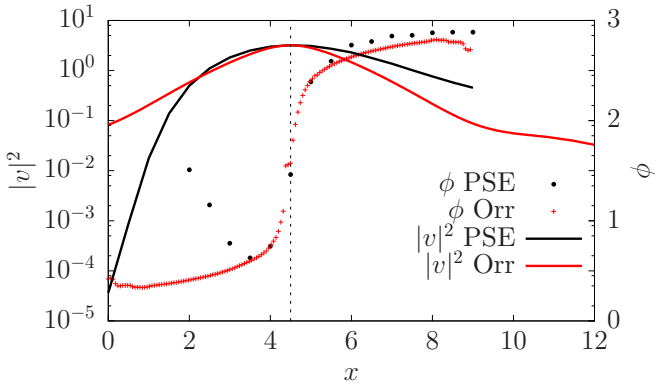

FIG. 10. Similar results to Fig. 8, comparing the linear PSE with the spatial Orr model for St = 0.5.

The Green's function $G(y,y',\alpha)$ has been determined by Case [9] and is given in Appendix B. The solution $\hat{\psi}(\alpha,y,\omega)$ is then found as

$$\hat{\psi}(\alpha,y,\omega) = \int_0^1 G(y,y',\alpha)\tilde{F}_2(y')2\pi\delta\left(\frac{\omega}{Sy'} - \alpha\right)dy'. \tag{A3}$$

Finally, performing the inverse Fourier transform in the streamwise direction, we obtain

$$\tilde{\psi}(x,y,\omega) = \frac{1}{2\pi}\int_{-\infty}^{+\infty}\int_0^1 G(y,y',\alpha)\tilde{F}_2(y')2\pi\delta\left(\frac{\omega}{Sy'} - \alpha\right)dy'e^{i\alpha x}d\alpha, \tag{A4}$$

which upon integration over α can be further simplified to

$$\tilde{\psi}(x,y,\omega) = \int_0^1 G\left(y,y',\frac{\omega}{Sy'}\right)\tilde{F}_2(y')e^{i(\omega x/Sy')}dy'. \tag{A5}$$

The role of the critical layer in the Orr mechanism can be seen in Eq. (A5). For each y position, the effect of the perturbation $\tilde{F}_2(y)$ considered at the critical layer fixes the response through the impulse response at that point (Green's function). The full response is the superimposition of these effects for all y.

We can note that the expression (A5) is a general form of Eq. (4) in the temporal Orr model of Jiménez [14]. The Green's function is in that case the one of the unbounded case $G(y,y',\alpha) = -\frac{1}{2\alpha}e^{-\alpha|y-y'|}$ (see Appendix B 1).

APPENDIX B: DETERMINATION OF THE GREEN'S FUNCTION

In order to find the Green's function of Eq. (A2), we consider that the homogeneous problem is solved left (index $\cdot_L$) and right (index $\cdot_R$) of the Dirac position y'. Solutions of the homogeneous problem

$$\left(-\alpha^2 + \frac{\partial^2 \cdot}{\partial y^2}\right)G(y,y',\alpha) = 0 \tag{B1}$$

are of the form

$$G = Ae^{\alpha y} + Be^{-\alpha y}. \tag{B2}$$

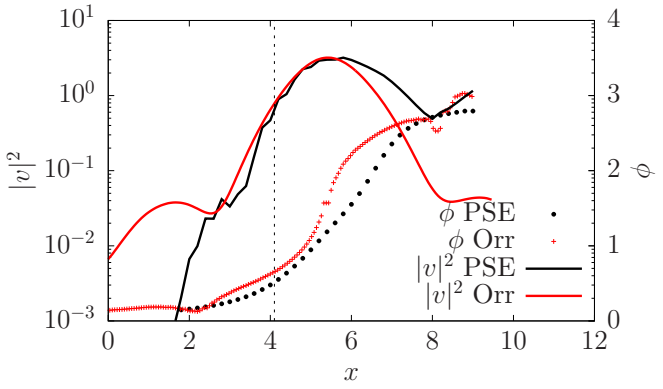

FIG. 11. Similar results to Fig. 7, comparing $\delta \boldsymbol{q}$ from the PSE with the spatial Orr model for St = 0.7.

Here A and B are chosen for each side of the Dirac such that continuity is ensured, the boundary conditions are satisfied, and

$$\lim_{\xi\to 0}\int_{y'-\xi}^{y'+\xi}\left(-\alpha^2+\frac{\partial^2.}{\partial y^2}\right)G(y,y',\alpha)dy=1\Rightarrow\frac{\partial G}{\partial y}(y'^{+},y')-\frac{\partial G}{\partial y}(y'^{-},y')=1. \tag{B3}$$

1. Unbounded case

For unbounded flow, boundary conditions are that disturbances cannot grow indefinitely as $y\to\pm\infty$. Hence, we must have $B_L=0$ and $A_R=0$ if $\alpha>0$, and $A_L=0$ and $B_R=0$ if $\alpha<0$. Continuity leads to

$$G(y,y',\alpha)=Ce^{-|\alpha||y-y'|} \tag{B4}$$

and Eq. (B3) gives $C=-\frac{1}{2\alpha}$.

2. Bounded case

Following now Case [9], $G(0,y',\alpha)=0$ leads to $A_L+B_L=0$ and then

$$G_L(y,y',\alpha)=C\sinh(\alpha y). \tag{B5}$$

For the right part, Eq. (B2) can be rewritten as

$$G_R=A'_Re^{\alpha(1-y)}+B'_Re^{-\alpha(1-y)} \tag{B6}$$

and $G(1,y',\alpha)=0$ leads to

$$G_R(y,y',\alpha)=D\sinh[\alpha(1-y)]. \tag{B7}$$

Case [9] showed that the appropriate constants for respecting continuity and Eq. (B3) are

$$C=-\frac{\sinh[\alpha(1-y')]}{\alpha\sinh(\alpha)},\quad D=-\frac{\sinh(\alpha y')}{\alpha\sinh(\alpha)}. \tag{B8}$$

APPENDIX C: RESULTS FOR OTHER STROUHAL NUMBERS

Figures 9–12 contain plots similar to Figs. 7 and 8 for two other Strouhal numbers: St = 0.5 and St = 0.7. Behavior similar to that at St = 0.6 is observed, which reinforces the interpretations made in the text. At St = 0.5 for the forced PSE in Fig. 9, the match of $|v|^2$ is not as good because the wave packet extends farther downstream.

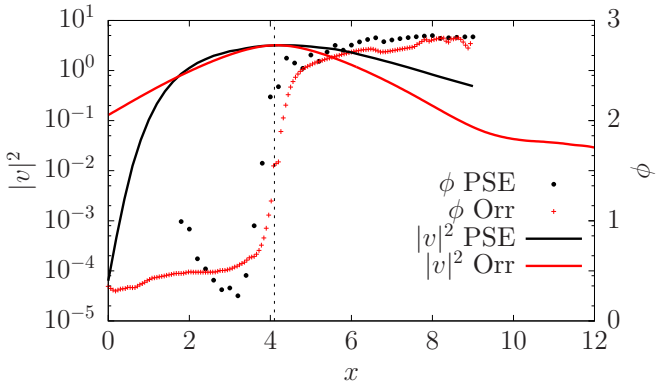

FIG. 12. Similar results to Fig. 8, comparing the linear PSE with the spatial Orr model for St = 0.7.

We did not display lower Strouhal numbers because wave packets have a longer spatial extent and then the relevant downstream region, where the Kelvin-Helmholtz mode becomes stable, occurs too far downstream. Thus, we could not check the model validity for these lower St due to a too short window in the axial direction in the experimental data. Higher Strouhal numbers were not used either because we could not compare with PIV data in [7] due to aliasing issues of experimental data [2]. We expect the Orr model to work in a wider range since linear models succeed in predicting the linear wave packets well above St = 0.7 [24]. Moreover, limitations of the Orr model are relaxed at higher frequencies since, due to the scaling $\frac{\omega x}{Sy}$, it is easier to ensure that the base flow is slowly divergent in the wavelength scale.

[1] P. Jordan and T. Colonius, Wave packets and turbulent jet noise, Annu. Rev. Fluid Mech. **45**, 173 (2013).
[2] A. V. G. Cavalieri, D. Rodriguez, P. Jordan, T. Colonius, and Y. Gervais, Wavepackets in the velocity field of turbulent jets, J. Fluid Mech. **730**, 559 (2013).
[3] Y. B. Baqui, A. Agarwal, A. V. G. Cavalieri, and S. Sinayoko, A coherence-matched linear source mechanism for subsonic jet noise, J. Fluid Mech. **776**, 235 (2015).
[4] A. V. G. Cavalieri, P. Jordan, A. Agarwal, and Y. Gervais, Jittering wave-packet models for subsonic jet noise, J. Sound Vib. **330**, 4474 (2011).
[5] D. Rodríguez, A. V. G. Cavalieri, T. Colonius, and P. Jordan, A study of linear wavepacket models for subsonic turbulent jets using local eigenmode decomposition of PIV data, Eur. J. Mech. B **49**, 308 (2015).
[6] M. Zhang, Linear and nonlinear waves in subsonic turbulent jets, Ph.D. thesis, Université de Poitiers, 2016.
[7] G. Tissot, M. Zhang, F. C. Lajús, A. V. G. Cavalieri, and P. Jordan, Sensitivity of wavepackets in jets to nonlinear effects: The role of the critical layer, J. Fluid Mech. **811**, 95 (2017).
[8] W. M. Orr, The stability or instability of the steady motions of a perfect liquid and of a viscous liquid. Part I: A perfect liquid, Proc. R. Irish Acad. A: Math. Phys. Sci. **27**, 9 (1907).
[9] K. M. Case, Stability of inviscid plane Couette flow, Phys. Fluids **3**, 143 (1960).
[10] P. G. Drazin and W. H. Reid, *Hydrodynamic Stability* (Cambridge University Press, Cambridge, 2004).
[11] P. J. Schmid and D. S. Henningson, *Stability and Transition in Shear Flows* (Springer, Berlin, 2001), Vol. 142.
[12] B. Farrell, Developing disturbances in shear, J. Atmos. Sci. **44**, 2191 (1987).
[13] J. Jiménez, How linear is wall-bounded turbulence? Phys. Fluids **25**, 110814 (2013).
[14] J. Jiménez, Direct detection of linearized bursts in turbulence, Phys. Fluids **27**, 065102 (2015).

[15] D. Sipp and O. Marquet, Characterization of noise amplifiers with global singular modes: The case of the leading-edge flat-plate boundary layer, Theor. Comput. Fluid Dyn. **27**, 617 (2013).
[16] G. Dergham, D. Sipp, and J.-C. Robinet, Stochastic dynamics and model reduction of amplifier flows: The backward facing step flow, J. Fluid Mech. **719**, 406 (2013).
[17] X. Garnaud, L. Lesshafft, P. J. Schmid, and P. Huerre, The preferred mode of incompressible jets: Linear frequency response analysis, J. Fluid Mech. **716**, 189 (2013).
[18] T. Herbert, Parabolized stability equations, Annu. Rev. Fluid Mech. **29**, 245 (1997).
[19] K. Gudmundsson, Instability wave models of turbulent jets from round and serrated nozzles, Ph.D. thesis, California Institute of Technology, 2010.
[20] K. Sasaki, S. Piantanida, A. V. G. Cavalieri, and P. Jordan, Real-time modelling of wavepackets in turbulent jets, J. Fluid Mech. **821**, 458 (2017).
[21] G. A. Faranosov, I. V. Belyaev, V. F. Kopiev, M. Y. Zaytsev, A. A. Aleksentsev, Y. V. Bersenev, V. A. Chursin, and T. A. Viskova, Adaptation of the azimuthal decomposition technique to jet noise measurements in full-scale tests, AIAA J. **55**, 572 (2017).
[22] B. J. McKeon and A. S. Sharma, A critical-layer framework for turbulent pipe flow, J. Fluid Mech. **658**, 336 (2010).
[23] R. S. Lindzen, Instability of plane parallel shear flow (toward a mechanistic picture of how it works), Pure Appl. Geophys. **126**, 103 (1988).
[24] A. V. G. Cavalieri, K. Sasaki, O. Schmidt, T. Colonius, P. Jordan, and G. A. Brès, High-frequency wavepackets in turbulent jets, in *Proceedings of the 22nd AIAA/CEAS Aeroacoustics Conference and Exhibit* (AIAA, Reston, VA, 2016), Paper AIAA 2016-3056.